

RobustMVS: Single Domain Generalized Deep Multi-view Stereo

Hongbin Xu Weitao Chen Baigui Sun Xuansong Xie Wenxiong Kang*

Abstract—Despite the impressive performance of Multi-view Stereo (MVS) approaches given plenty of training samples, the performance degradation when generalizing to unseen domains has not been clearly explored yet. In this work, we focus on the domain generalization problem in MVS. To evaluate the generalization results, we build a novel MVS domain generalization benchmark including synthetic and real-world datasets. In contrast to conventional domain generalization benchmarks, we consider a more realistic but challenging scenario, where only one source domain is available for training. The MVS problem can be analogized back to the feature matching task, and maintaining robust feature consistency among views is an important factor for improving generalization performance. To address the domain generalization problem in MVS, we propose a novel MVS framework, namely RobustMVS¹. A Depth-Clustering-guided Whitening (DCW) loss is further introduced to preserve the feature consistency among different views, which decorrelates multi-view features from viewpoint-specific style information based on geometric priors from depth maps. The experimental results further show that our method achieves superior performance on the domain generalization benchmark².

Index Terms—Multi-view Stereo, Domain Generalization, Deep Learning, 3D Reconstruction, Computer Vision

I. INTRODUCTION

MULTI-VIEW Stereo (MVS) is a long-standing elementary problem in computer vision, which aims to reconstruct 3D scenarios from multi-view images. In recent years, immense progress in this field has been witnessed since the advent of learning-based MVS. Typically, a MVS network [1] extracts multi-view image features with a shared CNN first and constructs cost volume via plane sweep algorithm [2] where source images are reprojected to the reference view frustum. Afterward, this cost volume is further regularized by 3D CNN [3]–[5] or recurrent neural networks [6]. Despite the amazing reconstruction performance and efficiency of learning-based MVS methods, the hunger for large-scale 3D annotations limits the application in realistic scenarios. Consequently, some unsupervised MVS methods [7]–[9] are

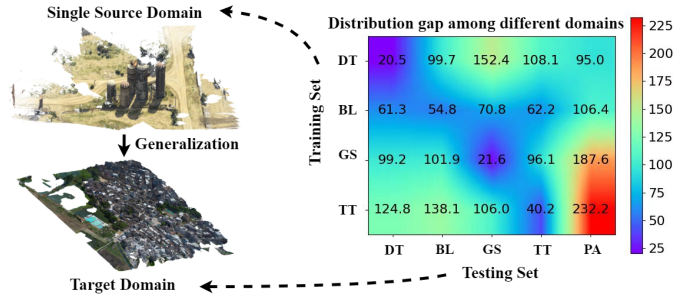


Fig. 1. Illustration of the proposed MVS domain generalization task. A single source domain is selected for training, and further tested on target domains without finetuning. The MMD Distances among datasets are visualized on the right hand. MVS datasets: DTU (DT) [11], BlendedMVS (BL) [12], GTASFM (GS) [13], PASMVS (PA) [14], Tanks&Temples (TT) [15].

further proposed to handle this issue without accessing ground truth.

In previous state-of-the-art methods, much effort has been devoted to making more accurate and complete reconstruction results, but relatively little has been put into understanding the domain generalization problem in MVS. In this paper, we aim to investigate the issue of generalizing to unseen domains in multi-view stereo (MVS), particularly the variations in illuminance among different domains. Specifically, we focus on a realistic and challenging scenario where there is only one source domain available but the goal is to generalize to target domains without any fine-tuning or adaptation, as illustrated in Fig. 1. The major difficulties lie in the large domain differences (visualized via MMD distance in Fig. 1) among different MVS datasets, including factors like variations of color, illumination, and texture. An interesting phenomenon can be found that the domain gap of **BL** \rightarrow **TT** is much smaller than the one of **DT** \rightarrow **TT**, which accounts for the better performance on **TT** test set when using **BL** as training set compared with **DT**, verifying the experiments in previous works [5], [10].

To handle the domain discrepancy, a common approach is to adapt the source domain distribution to the target domain distribution via domain adaptation (DA) techniques [17]–[20]. Whereas, it requires access to unlabeled samples in target domains, which limits their applicability in our MVS generalization task. A better reference is the domain generalization (DG) technique [21]–[23], which aims to learn domain-invariant representations. Furthermore, recent advances in the stereo matching task [24]–[30] have been developed to handle the domain generalization issue via conducting feature-level alignment for obtaining domain-invariant features. The stereo

*Corresponding author.

Hongbin Xu is with the School of Automation Science and Engineering, South China University of Technology, Guangzhou, China, 510641. Email: hongbinxu1013@gmail.com

Weitao Chen, Baigui Sun, and Xuansong Xie are with the Damo Academy, Alibaba Group, Hanzhou, China, 311121.

Wenxiong Kang is with the School of Automation Science and Engineering, South China University of Technology, Guangzhou, China, 510641 and Pazhou Lab, Guangzhou, China, 510335. Email: auwxkang@scut.edu.cn.

¹The code is released at: <https://github.com/ToughStoneX/Robust-MVS>.

²The MVS evaluation benchmark is released at: https://github.com/ToughStoneX/MVS_Evaluation_Benchmark

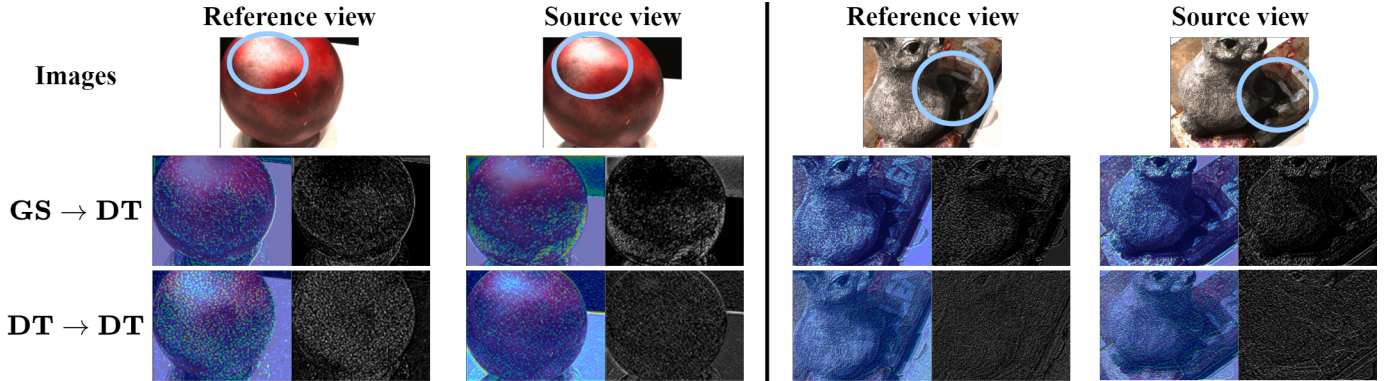


Fig. 2. Visualization of the activation map of CasMVSNet [3] via Grad-Cam [16]. **GS** \rightarrow **DT** means training on domain **GS** and generalizing to unseen domain **DT**. **DT** \rightarrow **DT** means training and testing on the same domain **DT**.

matching task can be viewed as a simplified case of MVS, which suffers less from view-point variations and shares more common regions. Instead of direct migration to the MVS case, we would like to take a step back first and revisit the bottleneck of generalization to unseen MVS domains.

To provide some inductive inspirations, we conduct a toy experiment that visualizes the feature activation map of an MVS network via modified Grad-CAM [16], as shown in Fig. 2. The first row shows the original multi-view images, and the following two rows respectively visualize the activation map when generalizing to unseen (**GS** \rightarrow **DT**) and seen (**DT** \rightarrow **DT**) domains. The non-activated regions (the blue circled area in Fig. 2) reveal the ignorance of MVS network during generalization. Consequently, the bottleneck of domain generalization in MVS can be resorted to the robustness of cross-view matching features across domain-specific conditions of illumination, color, and reflectance.

In this paper, we propose a novel MVS framework, RobustMVS, with minimum modification to the backbone MVS network. To handle the aforementioned issue that disturbs the feature consistency, we aim to suppress the domain-specific features and reserve the domain-invariant ones. As a series of studies [31]–[35] claims, feature covariance implies domain-specific style such as color and illumination. Based on this claim, the whitening transformation [27], [36] is a technique designed for removing feature correlation and thus enhancing the invariance to style variation. However, simply adopting the whitening transformation may not be applicable for MVS, because the whitening transformation decouples the feature style towards the whole image while MVS requires robust feature consistency among views in the local regions. Hence, we introduce a novel Depth-Clustering-guided Whitening (DCW) loss in the RobustMVS framework. With minor modifications to the MVS network, the last BN layer in each of the first 3 convolutional blocks is replaced with IN layer for normalization, as suggested by IBN-Net [37]. The whitening transformation is designed as a regularization loss without adding extra modules to the original network. Our DCW loss firstly clusters the merged sparse point clouds generated from multi-view depth annotations to find out common regions which are spatially close. Then the clusters are projected to

each view which determines the corresponding local regions in different views. By segmenting the local corresponding region (cluster) out, we warp the cross-view features to the same viewpoint via homography warping and calculate the feature covariance matrices on these correlated features. Then the feature whitening constraints are applied to enhance the domain-invariant features in these local correlated regions. Our experiments on MVS domain generalization task demonstrate the superior performance of the proposed framework.

The main contributions include the following:

- We systematically investigate the domain generalization problem in MVS and propose a new domain generalized benchmark across multiple datasets in MVS. Different from the original ones, the evaluation protocols (**BL/GS/GS**) are specially customized for measuring the performance of 3D reconstruction.
- We propose a novel domain generalized MVS framework, RobustMVS. By applying minor modifications to the MVS network and training with the proposed Depth-Clustering-guided Whitening (DCW) loss, the RobustMVS framework can improve the generalization ability with negligible computational cost.
- The domain generalized evaluation results show the superiority of our approach over existing approaches in both a qualitative and quantitative manner.

II. RELATED WORK

In this section, we briefly introduce the learning-based Multi-view Stereo (MVS) methods that are highly related to our paper. In addition, we also review some related work of Domain Generalization methods to explore the single domain generalization classification task and their relationship with our work.

A. Learning-based MVS

With the blessing of large-scale MVS datasets like DTU [11] and BlendedMVS [12], learning-based MVS methods are powered by deep convolutional networks [1], recurrent networks [6], and Transformers [10], achieving much better reconstruction accuracy and completeness than traditional MVS methods [38]–[40]. The pioneering work of MVSNet

[1] projects the feature maps of multi-view images extracted by CNN to the same reference view frustum, and builds a 3D cost volume to model the matching cost on each hypothetical depth plane. 3D CNN is then used for cost aggregation, and the output per-view depth maps are fused to construct a 3D point cloud. Due to the high memory and computation cost of MVSNet, lots of efforts have been proposed which can be divided into recurrent MVS networks and coarse-to-fine MVS networks. The recurrent methods [6], [41], [42] use the Recurrent Neural Network (RNN) to regularize the cost volume as an alternative to CNNs. In this way, the computational efficiency is sacrificed in exchange for reducing memory cost. When the coarse-to-fine methods [3], [4], [43]–[45] are adopted, the cost volume at the coarsest stage is constructed by uniformly sampling depth planes [46] of all depth hypotheses. Then the depth map is refined iteratively by building a more compact cost volume according to the estimated depth in previous stage as an initialization. CVP-MVSNet [43] proposes to adaptively determine the local depth search ranges by calculating the mean depth interval corresponding to 0.5 pixel distance on the epipolar line of the closest source images. UCSNet [4] utilizes the variance of the depth probability volume and depth residual to determine the pixel-wise depth interval when sampling depth hypotheses. UGNet [44] enables the MVS network to perceive the uncertainty, that is further used to guide the depth hypothesis sampling and build more compact cost volumes without redundancy. CasMVSNet [3] relies on the hyperparameters obtained from practice to determine the depth interval in coarse-to-fine cost volumes. Furthermore, some recent works [10], [47] attempt to embed MVS network with Transformer [48] backbones, achieving impressive improvement compared with previous methods. Another recent strand of work is unsupervised MVS [7]–[9], [49], [50], which designs self-supervised loss based on photometric consistency [51], [52] to train the MVS networks, producing competitive performance compared to supervised methods. Despite the promising results of learning-based MVS methods, the generalization problem in MVS has not been systematically explored yet. Though the generalization experiments to Tanks&Temples are widely used in previous methods, the experimental settings might vary because some methods [1], [6] adopt DTU as the source dataset while others utilize BlendedMVS [53] or multiple datasets [10]. As Fig. 1 shows, the distribution gap of BlendedMVS is much smaller than DTU, which might affect the final generalization performance when different source data settings are adopted. The exact influence of distribution among different MVS datasets has not been systematically investigated yet. More challenging but worthwhile, we introduce a novel domain generalization problem in MVS and aim to handle it in this paper.

B. Domain Generalization in Stereo Vision

Domain generalization [21]–[23] aims to learn from multiple source domains but generalize to unseen target domains. These techniques have also been extended to the era of stereo matching [24]–[27], which is a special case of MVS with horizontally aligned camera poses. DSMNet [25] adopts

a domain normalization layer to reduce shifts of domain-specific styles in images, and CFNet [26] proposes a fused cost volume representation that is robust to domain variations. FCStereo [27] involves selective whitening constraints to stereo matching to suppress the domain-sensitive features. The domain generalized stereo matching methods provide a reliable reference, and we extend the state-of-the-art methods to MVS network for comparison in Section V.

III. PRELIMINARY

In this section, we briefly introduce the concept of feature whitening transformation operation and its application to domain generalized tasks like Semantic segmentation and Stereo Matching in Section III-A. Then we discuss the limitation of the Whitening loss towards our MVS task in Section III-B.

A. Whitening Transformation and Whitening Loss

Denote that $\mathbf{F} \in \mathbb{R}^{C \times N_{HW}}$ is a flattened feature map, whose number of channels is C and $N_{HW} = H * W$. H and W respectively represent the height and width. As previous studies [31]–[35] claim, feature covariance matrix $\mathbf{F} \cdot \mathbf{F}^T \in \mathbb{R}^{C \times C}$ contains the visual style information of the whole image. Based on this intuition, whitening transformation (WT) is a linear transformation that aims to make the variance term of each channel in the feature map equal to one and the covariance term among different channels equal to zero. More concretely, it aims to find a whitened feature map $\tilde{\mathbf{F}} \in \mathbb{R}^{C \times N_{HW}}$ that satisfies $\tilde{\mathbf{F}} \cdot \tilde{\mathbf{F}}^T = N_{HW} \cdot \mathbf{I} \in \mathbb{R}^{C \times C}$, where \mathbf{I} is an identity matrix.

The mean vector of the feature map can be calculated as:

$$\boldsymbol{\mu} = \frac{1}{N_{HW}} \mathbf{F} \cdot \mathbf{1}, \mathbf{1} \in \mathbb{R}^{N_{HW} \times 1} \quad (1)$$

Then the covariance matrix can be computed as:

$$\boldsymbol{\Sigma} = \frac{1}{N_{HW}} (\mathbf{F} - \boldsymbol{\mu} \cdot \mathbf{1}^T) (\mathbf{F} - \boldsymbol{\mu} \cdot \mathbf{1}^T)^T, \mathbf{1} \in \mathbb{R}^{1 \times N_{HW}} \quad (2)$$

Afterwards, the solution of whitened feature map is:

$$\tilde{\mathbf{F}} = \boldsymbol{\Sigma}^{-\frac{1}{2}} (\mathbf{F} - \boldsymbol{\mu} \cdot \mathbf{1}^T), \mathbf{1} \in \mathbb{R}^{1 \times N_{HW}} \quad (3)$$

The covariance matrix $\boldsymbol{\Sigma}$ can be eigen-decomposed to $\mathbf{Q}\boldsymbol{\Lambda}\mathbf{Q}^T$, where $\mathbf{Q} \in \mathbb{R}^{C \times C}$ is the orthogonal matrix of eigenvectors, and $\boldsymbol{\Lambda} \in \mathbb{R}^{C \times C}$ is the diagonal matrix that contains eigenvalues. The inverse square root of the covariance matrix can be calculated with $\boldsymbol{\Sigma}^{-\frac{1}{2}} = \mathbf{Q}\boldsymbol{\Lambda}^{-\frac{1}{2}}\mathbf{Q}^T$, substituting the corresponding term in Eq. 3.

Since computing whitening transformation matrix analytically during inference is computationally expensive, GDWCT [54] converts the whitening constraints to a regularization loss on feature maps:

$$L_{\text{whiten}} = \mathbb{E}[\|\boldsymbol{\Sigma} - \mathbf{I}\|_1] \quad (4)$$

The whitening loss L_{whiten} and the costful computation process of calculating eigendecomposition are only used during training, while no extra computation is conducted during inference.

B. Limitations of Whitening Loss in MVS

With the nature of removing style information [55], the whitening constraints can be appended to the domain generalization task for learning domain-invariant representations. Whereas the domain-specific and domain-invariant features are simultaneously encoded in the covariance matrix of feature maps, they may be diminished by whitening loss at the same time. Some extensions [27], [36] handle this by selecting the domain-specific and domain-invariant terms of the covariance matrix via its sensitivity to changes like photometric transformations. However, these whitening losses are operated on the whole image to regularize the style difference among all pixels in the whole image. It is in conflict with the core target of MVS, which concentrates on the correspondence among pixels in local regions rather than the whole image. As the discussion in Section I of Fig. 2 reveals, the robustness of local corresponding features among views towards changes is the bottleneck when generalizing to unseen domains. Hence, instead of concentrating on the whole image with whitening loss, we propose a novel Depth-Clustering-guided Whitening (DCW) loss that applies whitening loss to the local corresponding regions of all views.

IV. METHOD

In this section, we design a novel RobustMVS framework to handle the domain generalized problem in MVS. In Section IV-A, we investigate the potential challenges of the domain generalized problem in MVS. Then, we introduce the adopted backbone network of the MVS framework in Section IV-B. In Section IV-C, we introduce the modification of MVS networks to support the feature whitening operations. Afterwards, we introduce the Depth-Clustering-guided Whitening (DCW) loss of this work which aims to conduct feature whitening selectively on the local corresponding regions among different views.

A. Problem Statement and Notation

We first introduce the notations and definition of the domain generalization problem in MVS. The goal of our MVS domain generalization task is to learn a model that is trained only using data from a source domain that can generalize well to the unseen target domain. In the source domain, given a pair of multi-view images with N views, the image on reference view is noted as $I_{\text{ref}} = I_1$, and the source view image is denoted as $I_{\text{src}} = \{I_v\}_{v=2}^N$. In the same way, the intrinsic and extrinsic matrix are written as: $K_{\text{ref}}/K_{\text{src}}$, $T_{\text{ref}}/T_{\text{src}}$. Accordingly, the ground truth depth map is written as $D_{\text{ref}}/D_{\text{src}}$.

B. Backbone

As shown in the third row of Fig. 3, the backbone MVS network of RobustMVS is a multi-stage MVS network that follows a coarse-to-fine pipeline as discussed in Section II. In default, we choose the foundational CasMVSNet [3] as the backbone. On each view, the output feature map of the feature extraction network is projected to the reference view via homography warping. Based on the given depth

hypothesis either from initial settings or from the prediction of the previous stage, the cost volume is built to measure the similarity of corresponding points among views. Then the cost volume is fed to a 3D CNN in the cost regularization process, and finally outputs the predicted depth.

C. Convolutional Block with Normalization

The optimization of the aforementioned whitening loss in Eq. 4 can be separated into two parts: optimization on the diagonal and off-diagonal of the covariance matrix. Denote that F_i is channel i of feature map F . For the diagonal constraints, its loss can be written as: $\|\Sigma - 1\|_1 = \|\frac{F_i F_i^T}{N_{HW}} - 1\|_1$. For the off-diagonal constraints, its loss can be written as: $\|\Sigma\|_1 = \|\frac{F_i F_j^T}{N_{HW}}\|_1$. The former constraint forces the scale of channel F_i to be $\frac{1}{N_{HW}}$, while the latter constraint forces the target to be zero. This conflict may confuse the training process. Hence, a simple solution to handle this issue is to standardize the feature map with Instance Normalization [56] to ensure a fixed scale for each channel F_i :

$$\mathbf{F}_s = (\text{diag}(\Sigma))^{-\frac{1}{2}} \odot (\mathbf{F} - \boldsymbol{\mu} \cdot \mathbf{1}^T), \mathbf{1} \in \mathbb{R}^{1 \times N_{HW}} \quad (5)$$

where \odot is an element-wise multiplication. Then the normalized feature map can be used to compute the covariance matrix Eq. 2 and the whitening loss via Eq. 4

The summarized principle is that the whitening loss should be computed on the standardized output of an Instance Normalization layer. With this in mind, we replace the Batch Normalization layer with the Instance Normalization layer when the output feature map is used to calculate the whitening loss, as shown in Fig. 3.

D. Depth-Clustering-guided Whitening Loss

Since the core of MVS is the feature-matching task, which concentrates on the correspondence in local regions. It is inappropriate to directly append whitening constraints to features in the whole image, because it may diminish specific style patterns which is beneficial for feature consistency in local regions. Hence, we propose a novel Depth-Clustering-guided Whitening (DCW) loss to conduct feature whitening selectively on the local corresponding regions among different views. In this section, we first introduce the procedure of segmenting the local correspondence via clustering with depth priors in Sec. IV-D1, and then expound the feature whitening on cross-view corresponding features by homography warping in Sec. IV-D2.

1) *Clustering with Depth Priors*: As shown in the first row of Fig. 3, the ground truth depth maps of reference view ($D_{\text{ref}} \in \mathbb{R}^{H \times W}$) and source view ($D_{\text{src}} \in \mathbb{R}^{H \times W}$) are first projected back into 3D space.

$$P_{\text{ref}}^i = T_{\text{ref}}^{-1} K_{\text{ref}}^{-1} D_{\text{ref}}(p_{\text{ref}}^i) p_{\text{ref}}^i \quad (6)$$

$$P_{\text{src}}^j = T_{\text{src}}^{-1} K_{\text{src}}^{-1} D_{\text{src}}(p_{\text{src}}^j) p_{\text{src}}^j \quad (7)$$

where i and j are respectively the index of valid points in D_{ref} and D_{src} , and p_{ref} and p_{src} represent the 2D image coordinates. Denote that the number of valid pixels in the reference view

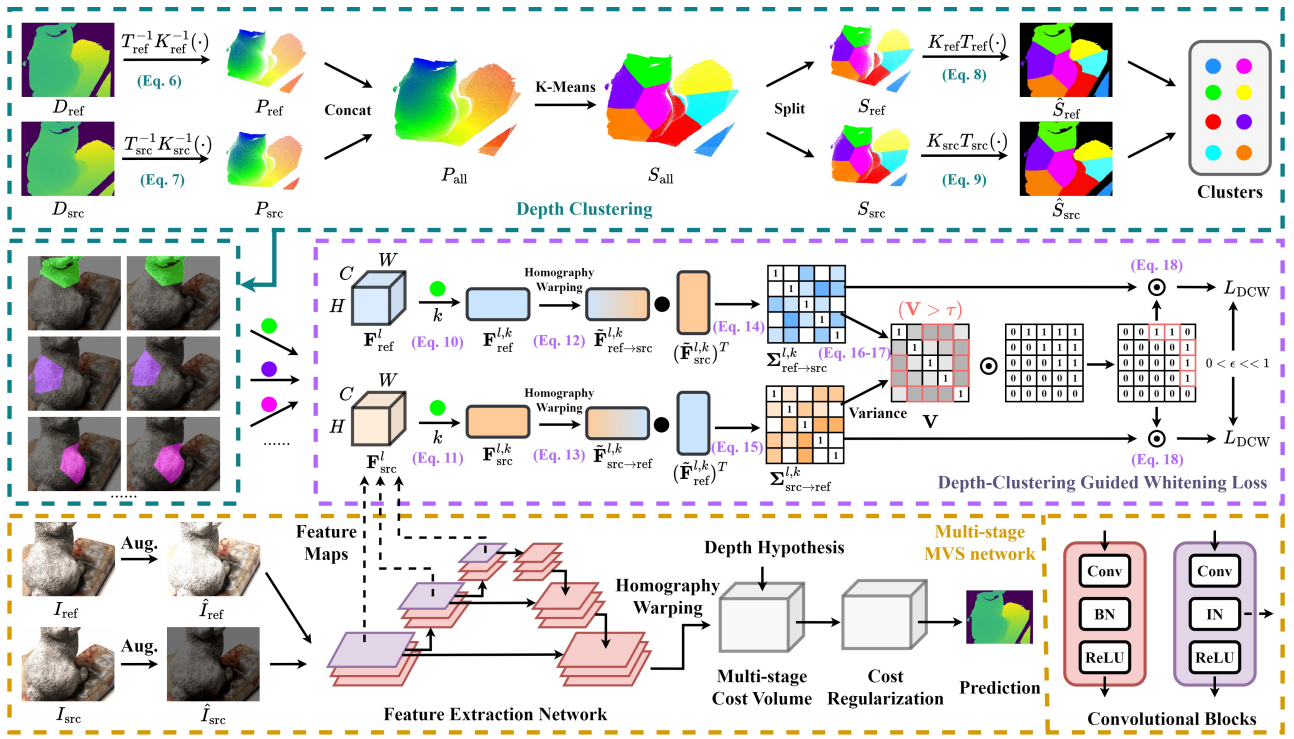


Fig. 3. Illustration of our proposed RobustMVS framework. Aug. means random data augmentation. The blue dashed box represents the clustering process with the depth prior. This process can extract local corresponding regions by clustering, and the clusters are further fed to the proposed Depth-Clustering Guided Whitening loss shown in the purple dashed box. The orange dashed box at the bottom represents the basic architecture of the adopted MVS network, in which the first 3 BN convolution blocks are replaced with the IN-based convolution blocks.

is M_{ref} and the one in the source view is M_{src} . The projected point cloud on reference view is $P_{\text{ref}} \in \mathbb{R}^{M_{\text{ref}} \times 3}$, and the point cloud on source view is $P_{\text{src}} \in \mathbb{R}^{M_{\text{src}} \times 3}$.

Then the point clouds P_{ref} and P_{src} are concatenated together to get a fused point cloud $P_{\text{all}} \in \mathbb{R}^{(M_{\text{ref}}+M_{\text{src}}) \times 3}$. Afterward, K-Means [57] is adopted to cluster the spatially neighboring regions of the fused point cloud P_{all} . The number of clusters is defined as K_{clu} , and the output clustered point cloud is $S_{\text{all}} \in \mathbb{R}^{(M_{\text{ref}}+M_{\text{src}}) \times K_{\text{clu}}}$. The K_{clu} channels of point cloud S_{all} use one-hot encoding to represent the K_{clu} clusters. Each of the K_{clu} clusters in point cloud S_{all} represents the spatially neighboring regions that bind the matching consistency of local regions between different views. Afterward, point cloud S_{all} can be split back into clusters on reference view and source view: $S_{\text{ref}} \in \mathbb{R}^{M_{\text{ref}} \times K_{\text{clu}}}$ and $S_{\text{src}} \in \mathbb{R}^{M_{\text{src}} \times K_{\text{clu}}}$. Note that the K_{clu} clusters in S_{ref} and S_{src} are corresponding regions that inherently model the matching consistency among views.

The clustered point clouds can then be projected into the 2D image space:

$$\tilde{S}_{\text{ref}}(p_{\text{ref}}^i) = S_{\text{ref}}(P_{\text{ref}}^i), p_{\text{ref}}^i = \pi(K_{\text{ref}} T_{\text{ref}} P_{\text{ref}}^i) \quad (8)$$

$$\tilde{S}_{\text{src}}(p_{\text{src}}^j) = S_{\text{src}}(P_{\text{src}}^j), p_{\text{src}}^j = \pi(K_{\text{src}} T_{\text{src}} P_{\text{src}}^j) \quad (9)$$

where $\pi([x, y, z]^T) = [x/z, y/z, 1]$, i and j are respectively the index of valid points which can be projected into 2D image. $\tilde{S}_{\text{ref}} \in \mathbb{R}^{H \times W \times K_{\text{clu}}}$ and $\tilde{S}_{\text{src}} \in \mathbb{R}^{H \times W \times K_{\text{clu}}}$ are 2D clustered segmentation maps that share common clusters among different views.

2) *Homography Whitening*: Denote that $\mathbf{F}_{\text{ref}}^l \in \mathbb{R}^{N_{HW} \times C}$ and $\mathbf{F}_{\text{src}}^l \in \mathbb{R}^{N_{HW} \times C}$ are the output feature maps on the l -th layer, which is normalized with Instance Normalization following Eq. 5. As shown in Fig. 3, each feature map \mathbf{F}_{s}^l is filtered with each of the K_{clu} clusters to find locally consistent regions:

$$\tilde{\mathbf{F}}_{\text{ref}}^{l,k} = \mathbf{F}_{\text{ref}}^l \odot \mathcal{K}(\tilde{S}_{\text{ref}}^k = 1) \quad (10)$$

$$\tilde{\mathbf{F}}_{\text{src}}^{l,k} = \mathbf{F}_{\text{src}}^l \odot \mathcal{K}(\tilde{S}_{\text{src}}^k = 1) \quad (11)$$

where \odot is an element-wise multiplication. $\tilde{\mathbf{F}}_{\text{ref}}^{l,k} \in \mathbb{R}^{M_{\text{ref}}^k \times C}$ and $\tilde{\mathbf{F}}_{\text{src}}^{l,k} \in \mathbb{R}^{M_{\text{src}}^k \times C}$ are the pixel-wise features of cluster k on the reference view and the source view. M_{ref}^k and M_{src}^k are the numbers of valid pixels in cluster K on reference view and source view.

Since M_{ref}^k and M_{src}^k are probably unequal, they can not be directly used to calculate the covariance matrix that has to be a square matrix. Hence, we reproject $\tilde{\mathbf{F}}_{\text{ref}}^{l,k}$ to the source view and $\tilde{\mathbf{F}}_{\text{src}}^{l,k}$ to the reference view via homography warping:

$$\tilde{\mathbf{F}}_{\text{ref} \rightarrow \text{src}}^{l,k}[p_{\text{src}}] = \tilde{\mathbf{F}}_{\text{ref}}^{l,k}[\pi(K_{\text{ref}} T_{\text{ref}} T_{\text{src}}^{-1} K_{\text{src}}^{-1} p_{\text{src}})] \quad (12)$$

$$\tilde{\mathbf{F}}_{\text{src} \rightarrow \text{ref}}^{l,k}[p_{\text{ref}}] = \tilde{\mathbf{F}}_{\text{src}}^{l,k}[\pi(K_{\text{src}} T_{\text{src}} T_{\text{ref}}^{-1} K_{\text{ref}}^{-1} p_{\text{ref}})] \quad (13)$$

where $\tilde{\mathbf{F}}_{\text{src} \rightarrow \text{ref}}^{l,k} \in \mathbb{R}^{M_{\text{ref}}^k \times C}$ and $\tilde{\mathbf{F}}_{\text{ref} \rightarrow \text{src}}^{l,k} \in \mathbb{R}^{M_{\text{src}}^k \times C}$ are the warped features via bilinear sampling to ensure the backward propagation of gradient during training.

Then we can calculate the covariance matrix:

$$\Sigma_{\text{ref} \rightarrow \text{src}}^{l,k} = (\tilde{\mathbf{F}}_{\text{src} \rightarrow \text{ref}}^{l,k})^T \tilde{\mathbf{F}}_{\text{ref} \rightarrow \text{src}}^{l,k} \quad (14)$$

$$\Sigma_{\text{src} \rightarrow \text{ref}}^{l,k} = (\tilde{\mathbf{F}}_{\text{ref} \rightarrow \text{src}}^{l,k})^T \tilde{\mathbf{F}}_{\text{src} \rightarrow \text{ref}}^{l,k} \quad (15)$$

where the covariance matrix $\Sigma_{\text{ref} \rightarrow \text{src}}^{l,k}$ and $\Sigma_{\text{src} \rightarrow \text{ref}}^{l,k}$ have the resolution of $C \times C$.

Note that the original input of the reference image and source image are randomly augmented with photometric transformations as shown in the left-bottom of Fig. 3. Here, the covariance matrix $\Sigma_{\text{ref} \rightarrow \text{src}}^{l,k}$ and $\Sigma_{\text{src} \rightarrow \text{ref}}^{l,k}$ models the style information on the local region of the same cluster k . With the random data augmentation, we would like to find out which elements of the covariance matrix is sensitive to changes, and suppress them with whitening loss. Formally, the variance matrix between these covariance matrices is calculated as follows:

$$\mu_{\Sigma} = \frac{\Sigma_{\text{ref} \rightarrow \text{src}}^{l,k} + \Sigma_{\text{src} \rightarrow \text{ref}}^{l,k}}{2} \quad (16)$$

$$\mathbf{V} = \frac{(\Sigma_{\text{ref} \rightarrow \text{src}}^{l,k} - \mu_{\Sigma})^2 + (\Sigma_{\text{src} \rightarrow \text{ref}}^{l,k} - \mu_{\Sigma})^2}{2} \quad (17)$$

where \mathbf{V} contains the variance of each covariance element across random data augmentation towards consistent regions on different views. Note that The random data augmentation transformations include the color jittering and gamma correction. Color jittering generates random variations of brightness, contrast, and saturation. The brightness and contrast factor are set to 0.7, and the one of saturation is set to 0.2. Gamma correction randomly samples gamma values within a range of 0.5-2.0 to augment the images.

As presented in the figure, we then filter out the sensitive element from \mathbf{V} with a threshold τ using the indicator function: $\mathcal{K}(\mathbf{V} > \tau)$. τ is an adaptive threshold calculated following [36] (Details are discussed in the appendix). Furthermore, since the covariance matrix is a symmetric matrix, only the upper triangle elements are useful for the whitening loss. Hence, we can calculate the mask given the upper triangle matrix $\text{triu}(\mathbf{1})$:

$$\mathbf{O} = \mathcal{K}(\mathbf{V} > \tau) \odot \text{triu}(\mathbf{1}), \mathbf{1} \in \mathbb{R}^{C \times C} \quad (18)$$

Finally, the DCW loss is defined as:

$$L_{\text{DCW}}^{l,k} = \mathbb{E}[\|\Sigma_{\text{ref} \rightarrow \text{src}}^{l,k} \odot \mathbf{O} - \epsilon\|_1 + \|\Sigma_{\text{src} \rightarrow \text{ref}}^{l,k} \odot \mathbf{O} - \epsilon\|_1] \quad (19)$$

where $0 < \epsilon \ll 1$ is set as a threshold aiming to relax the constraints of whitening loss during optimization. ϵ is added to avoid the unexpected failures (NaN values) caused by whitening loss.

3) *Overall loss*: The final training loss is a weighted sum of depth estimation loss in MVS and the proposed DCW loss:

$$L = L_{\text{depth}} + \frac{\lambda}{(N-1)LK} \sum_{n=1}^{N-1} \sum_{l=1}^L \sum_{k=1}^{K_{\text{clu}}} L_{\text{DCW}}^{l,k} \quad (20)$$

where L_{depth} is the commonly applied smooth huber loss following [3]. λ is the weight of DCW loss and is set to 1 in default. The N views of multi-view images are separated in $N-1$ paired samples comprised of reference view ($n=1$) and source view ($n=2, \dots, N$). L layers output standardized features to compute whitening loss, and K_{clu} clusters are used as shown in Fig. 3.

V. EXPERIMENT

A. Datasets

DTU (**DT**) [11] is an indoor MVS dataset. Each scene is taken from 49 positions and the image resolution is 1600×1200 . 7 different light conditions are included in each scene. Following the separation of MVSNet [1], 78 scenes are included in the training set, 17 scenes are used in the validation set, and 21 scenes are used in the test set.

BlendedMVS (**BL**) [12] is a large-scale MVS dataset, which contains various scenes, including architectures, sculptures, and small objects. Following their official split³, 106 scenes are used in the training set and 7 scenes are used in the evaluation set.

GTASFM (**GS**) [13] is a synthetic dataset collected from GTA-V, a famous video game with realistic scenarios. Following the official split, 200 scenes are included in the training set, and 19 scenes are included in the test set. The original images provided in **GS** are a sequence of images extracted from a video, paired with camera parameters and ground truth depth maps. To support the format of MVS networks, these image sequences are firstly processed with COLMAP and the neighboring images are selected based on the similarity score of matching pixels among views. The format is saved following the format⁴ defined in the open-source code of MVSNet.

Tanks&Temples (**TT**) [15] is a large-scale MVS dataset collected in outdoor scenes with realistic conditions. It contains 7 scenes in the training set, 8 scenes in the Intermediate evaluation set, and 6 scenes in the Advanced evaluation set. Following the preprocessed evaluation set provided by MVSNet, we use both the Intermediate and Advanced sets for evaluation. However, no processed training set is available in the open-source codes of MVS methods. Hence, we further use COLMAP to sparsely reconstruct scenes on the training set of **TT**, and separate the neighboring views based on the similarity of matching points in different views. More importantly, the depth annotations are not provided in the training set of **TT**, hence we render the densely reconstructed point clouds of all scenes via COLMAP to obtain the depth map on each view. Our processed training set of **TT** is used as a candidate for source domains, and the evaluation set provided by MVSNet is used as a candidate for target domain.

PASMVS (**PA**) [14] is a perfectly accurate synthetic MVS dataset⁵, consisting of 400 scenes with ground truth depth maps and camera parameters. Each scene is composed of a unique combination of different camera focal lengths, geometrical models, environmental textures, and materials. The material properties are primarily specular, which simulate different light conditions with different diffuse materials. Here we utilize the test set of **PA** as an extra evaluation dataset while selecting target domains.

³<https://github.com/YoYo000/BlendedMVS>

⁴https://github.com/YoYo000/MVSNet/blob/master/mvsnet_colmap2mvsnet.py

⁵<https://github.com/andrebroekman/PASMVS>

B. MMD Difference among Datasets

In Fig. 1, the MMD distances among different source domains and target domains are visualized to reveal the difference among various MVS datasets. To calculate the MMD distance, we use a pre-trained VGG network to compute the embedding feature of all images in the domain. Each image in the MVS training/testing set is converted into a feature vector with 4096 channels. All these feature vectors are concatenated together to construct a feature matrix describing the corresponding domain. Then, we can calculate the MMD distance with these feature matrices to assess the distribution gap among different MVS datasets.

From the presented results in Fig. 1, several interesting phenomena can be found:

- Compared with the training set of **DT**, the training set of **BL** has a much smaller distribution gap towards the evaluation set of **TT** ($\mathbf{BL} \rightarrow \mathbf{TT}$: 62.2; $\mathbf{DT} \rightarrow \mathbf{TT}$: 108.1). This explains the fact that the performance of MVS models trained on **BL** is better than the models trained on **DT**, which is also revealed by previous works [5], [10]. Furthermore, it means that the impressive generalization results of many recent methods on **TT** benchmark may not be totally convincing, because the performance improvement may be dependent on the benefit of the large-scale dataset with a small distribution gap like **BL**, even the joint training of **BL** and **DT**. Consequently, we investigate the domain generalization MVS problem in this paper and restrict the setting of generalization with only one single domain to diminish the aforementioned confounding factor.
- The additional evaluation set of **PA** has much higher distribution gap compared with other target domains. Note that **PA** simulates various conditions of object materials and light conditions, which naturally possesses larger difference compared with other target domains. Since **DT** models 7 different light conditions in each scene, the distribution gap of $\mathbf{DT} \rightarrow \mathbf{PA}$ is much smaller than the ones of other source domains. Consequently, the illuminance is also an important factor that differs different MVS dataset between $\mathbf{DT/PA}$ and $\mathbf{BL/GS/TT}$.

C. 3D Ground Truth and Evaluation Benchmark

Although **DT** and **TT** contain their own 3D reconstruction evaluation benchmarks, the remaining datasets **BL**, **GS**, and **PA** do not have similar benchmarks for 3D reconstructed results. Hence, we also need to design customized quantitative benchmarks to measure the performance of 3D reconstruction. To assess the reconstruction quality quantitatively, collecting the 3D ground truth is indispensable for the evaluation of MVS 3D reconstruction. Hence, we need to prepare the 3D ground truth of each scene in the target domains and propose an equitable evaluation metric to measure the reconstruction results.

1) *DT Evaluation*: For **DT**, the ground truth and official evaluation benchmark are provided in the official website⁶.

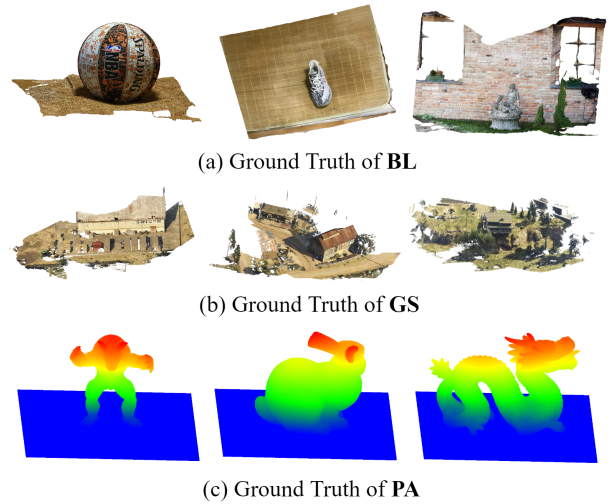


Fig. 4. Some examples of the processed ground truths of **BL/GS/PA**.

During the evaluation, the metric of Accuracy, Completeness, and Overall are used to measure the reconstruction results. Accuracy is used to measure the average distance from the reconstructed point clouds to the ground truth point clouds. Completeness is used to measure the average distance from the ground truth point clouds to the reconstructed point clouds. Overall is the average of Accuracy and Completeness, which is used as an overall assessment of the reconstruction quality.

2) *TT Evaluation*: For **TT**, the ground truth is not available, and the official evaluation benchmark requires submission of reconstructed point clouds to their official website⁷. The test set is separated into 2 parts: the Intermediate set and the Advanced set. F-score on each scene is used to measure the reconstruction quality.

3) *BL/GS/PA Evaluation*: For **BL/GS/PA**, we have to prepare the ground truth and build the evaluation benchmark by ourselves, since no existing evaluation benchmark is available in the open-source community.

To get the 3D ground truth, we need to process **BL/GS/PA** differently:

- For **BL**, the provided ground truth mesh is comprised of various splits. The mesh parts are first merged to construct the complete mesh as ground truth. Then, we utilize Monte-Carlo sampling to uniformly sample point cloud from the ground truth mesh. The sampled point cloud in each scene is used as 3D ground truth in the following evaluation stage. Some examples of the sampled ground truth point cloud are shown in Fig. 4(a).
- For **GS**, the ideally accurate depth maps and camera parameters are fused with Gipuma [38] to construct the ground truth point cloud. It is noted that the extrinsic matrix in GTASFM is the inverse form of the ones defined in Gipuma. Some examples of the ground truth are visualized in Fig. 4(b).
- For **PA**, the provided ground truth is 3d mesh template without texture. We utilize Monte-Carlo sampling to uniformly sample the ground truth point cloud from the

⁶http://roboimagedata.compute.dtu.dk/?page_id=36

⁷<https://www.tanksandtemples.org/>

original mesh. Some examples of the ground truth points are shown in Fig. 4(c).

To construct the evaluation benchmark, we follow the evaluation protocol defined by **TT** [15] and [58], which uses Precision, Recall, and F-score to measure the reconstruction quality.

Denote that the ground truth point cloud is $P_G \in \mathbb{R}^{M \times 3}$, and the reconstructed point cloud is $P_R \in \mathbb{R}^{N \times 3}$. Following the definition of Chamfer Distance (CD), we can have:

$$D_{CD} = \frac{1}{M} \sum_{p_m \in P_G} \min_{p_n \in P_R} \|p_m - p_n\|_2^2 + \frac{1}{N} \sum_{p_n \in P_R} \min_{p_m \in P_G} \|p_m - p_n\|_2^2 \quad (21)$$

where p_m is any point of ground truth point cloud P_G , and p_n is any point of reconstructed point cloud P_R . We can divide Eq. 21 into 2 terms:

$$D_{G \rightarrow R} = \frac{1}{M} \sum_{p_m \in P_G} \min_{p_n \in P_R} \|p_m - p_n\|_2^2 \quad (22)$$

$$D_{R \rightarrow G} = \frac{1}{N} \sum_{p_n \in P_R} \min_{p_m \in P_G} \|p_m - p_n\|_2^2 \quad (23)$$

where Eq. 22 represents the average distance of all points in the ground truth point cloud P_G towards the reconstructed point cloud P_R , which can be viewed as a measure of completeness. And Eq. 23 represents the average distance of all points in the reconstructed point cloud P_R towards the ground truth point cloud P_G , which can be treated as a measure of accuracy.

The calculated distances can further be aggregated to define the recall and precision given a threshold d :

$$\text{Reca}(d) = \frac{100}{M} \sum_{p_m \in P_G} [\min_{p_n \in P_R} \|p_m - p_n\|_2^2 < d] \quad (24)$$

$$\text{Prec}(d) = \frac{100}{N} \sum_{p_n \in P_R} [\min_{p_m \in P_G} \|p_m - p_n\|_2^2 < d] \quad (25)$$

where $[\]$ is the Iverson bracket. The definition of Recall and Precision are respectively provided in Eq. 24 and Eq. 25.

The definition of F-score can be calculated from Recall and Precision:

$$\text{F-score}(d) = \frac{2\text{Prec}(d)\text{Reca}(d)}{\text{Prec}(d) + \text{Reca}(d)} \quad (26)$$

Note that F-score, Precision, and Recall are defined to lie in the range of $[0 - 100]$. The higher these scores are, the better the performance is.

D. Network Details

We implement our method in PyTorch and train the models with 4 NVIDIA A-100 GPUs. The default setting is the same as the backbone network. For the hyper-parameter settings, $\lambda = 1.0$, $K = 8$, $\epsilon = 0.02$. The number of adopted layers is set to 3. We train the network for 24 epochs on **DT**, **BL**, **GS**, and 32 epochs on **TT**. Since the training set of **TT** is smaller than the others, we maintain a fixed range of iterations

by increasing the epochs a little. The number of clusters on depth map is set to 8 in default. If not mentioned, the adopted setting in training is the same as the one of the backbone MVS network.

E. Comparison with MVS methods

In Table I, we compare the quantitative performance on domain generalization with other state-of-the-art MVS methods. Only the training set of **DT** is selected as source domain to train the model, and we evaluate the performance on other source domains. We directly utilize the open-sourced pre-trained model of CasMVSNet [3], PatchMatchNet [59], IterMVS [60], MVSTER [47], CDS-MVSNet [61], and UniMVSNet [5], to test on target domains without finetuning. These pre-trained models are further used for evaluation on unseen datasets on **DT** \rightarrow **BL**, **DT** \rightarrow **GS**, and **DT** \rightarrow **PA**. We further provide experimental results on the same dataset (**DT** \rightarrow **DT**) to evaluate the performance. In the table, RobustMVS-Cas means that the CasMVSNet is selected as the backbone of our RobustMVS framework. In analogy, RobustMVS-Iter means that the IterMVS is selected as the backbone network. The metric of F-score reflects the overall performance of 3D reconstruction. The best results are in bold, and the second best is marked with underline.

An interesting phenomenon can be found that these state-of-the-art models in comparison may fail to generalize to other domains (**BL**, **GS**, **PA**) well even with impressive performance on DT. The reason is that their parameters are highly tuned to fit well-used datasets DT or **TT** with human efforts, resulting in overfitting effect to some extent when a novel unseen domain is involved. Smaller models like CasMVSNet, PatchMatchNet, and IterMVS suffer less from the overfitting issue. Comparing with state-of-the-art MVS methods, our RobustMVS-Cas and RobustMVS-Iter achieves better performance on all 3 cross-domain tracks. As the results show, our proposed method can effectively reduce the performance degradation in unseen novel domains. Comparing with the baseline method with same backbone (CasMVSNet / IterMVS), our RobustMVS-Cas and RobustMVS-Iter can improve the generalization performance effectively on all 3 cross-domain tracks. It shows that our proposed RobustMVS can improve the generalization performance when combined with different MVS backbones. For qualitative results, we provide the visualization comparisons in Fig. 5. Some examples under **DT** \rightarrow **BL** and **DT** \rightarrow **GS** are selected for visualization. The reconstructed point clouds of RobustMVS-Cas is compared with CDS-MVSNet and MVSTER in the figure. From the figure, we can find that our method can achieve more accurate and complete reconstruction than these state-of-the-art MVS methods. Furthermore, the proposed method can achieve slightly better reconstruction performance on RobustMVS-Cas and RobustMVS-Iter compared with the baseline CasMVSNet and IterMVS. It shows that our RobustMVS can preserve great performance in the same domain (**DT** \rightarrow **DT**) meantime increasing the generalization ability towards other domains (**DT** \rightarrow **BL/GS/PA**).

TABLE I

QUANTITATIVE COMPARISONS WITH THE-STATE-OF-ART MVS METHODS UTILIZING **DT** AS SOURCE DOMAIN. NOTE THAT ALL MODEL IS PURELY TRAINED BY **DTU** TRAINING SET, AND TESTED ON OTHER DATASETS WITHOUT ANY FINETUNING. BEST RESULTS ARE IN BOLD, SECOND BEST ARE UNDERLINED.

| Methods | DT \rightarrow DT | | | DT \rightarrow BL | | | DT \rightarrow GS | | | DT \rightarrow PA | | |
|-----------------------|-----------------------------------|--------------------|----------------------|-----------------------------------|------------------|--------------------|-----------------------------------|------------------|--------------------|-----------------------------------|------------------|--------------------|
| | Acc. \downarrow | Comp. \downarrow | Overall \downarrow | Prec. \uparrow | Reca. \uparrow | F-score \uparrow | Prec. \uparrow | Reca. \uparrow | F-score \uparrow | Prec. \uparrow | Reca. \uparrow | F-score \uparrow |
| MVSNet [1] | 0.396 | 0.527 | 0.462 | 29.86 | 25.68 | 22.42 | 16.17 | 18.94 | 16.74 | 20.36 | 24.21 | 21.44 |
| CasMVSNet [3] | 0.325 | 0.385 | 0.355 | 48.21 | 39.91 | 39.06 | 42.99 | 36.93 | 38.74 | 42.61 | 41.76 | 40.78 |
| PatchMatchNet [59] | 0.427 | 0.277 | 0.352 | 41.15 | 49.34 | 41.69 | 49.47 | 38.25 | 42.66 | 30.12 | 40.42 | 33.95 |
| IterMVS [60] | 0.373 | 0.354 | 0.363 | 47.21 | 43.93 | 41.79 | 47.36 | 36.91 | 40.92 | 45.00 | 44.84 | 44.37 |
| MVSTER [47] | 0.350 | 0.276 | 0.313 | 41.29 | 40.60 | 36.26 | 24.86 | 18.64 | 20.75 | 33.50 | 52.28 | 40.45 |
| CDS-MVSNet [61] | 0.352 | 0.280 | 0.316 | 43.74 | 33.97 | 33.89 | 22.45 | 22.71 | 21.66 | 29.09 | 20.92 | 23.72 |
| UniMVSNet [5] | 0.352 | 0.278 | <u>0.315</u> | 49.09 | 35.06 | 37.93 | 54.30 | 30.66 | 38.47 | 64.46 | 22.07 | 32.24 |
| RobustMVS-Cas | 0.328 | 0.365 | 0.346 | 52.07 | 42.91 | <u>42.72</u> | 45.45 | 44.08 | 43.85 | 56.74 | 49.99 | 52.03 |
| RobustMVS-Iter | 0.315 | 0.406 | 0.361 | 49.17 | 43.97 | 43.13 | 51.32 | 39.11 | 43.83 | 49.93 | 44.87 | 45.89 |

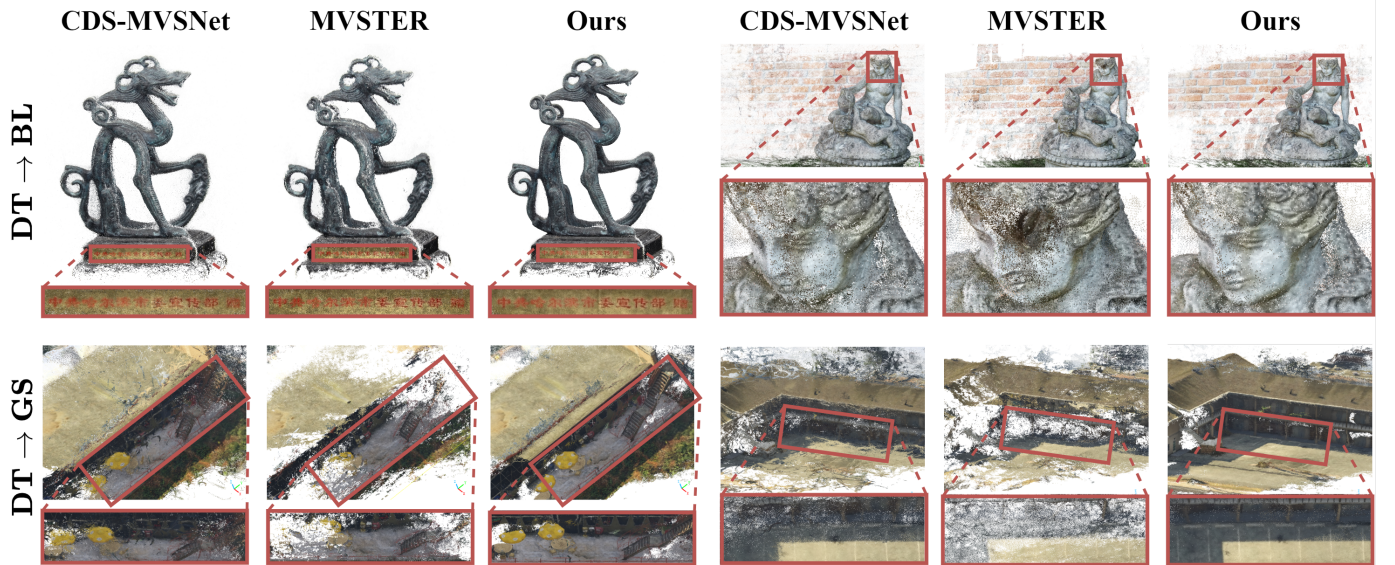


Fig. 5. Qualitative comparisons with state-of-the-art MVS methods utilizing **DT** as source domain.

F. Comparison with DG methods

In Table II, we provide the quantitative comparison between our method and other domain generalization methods. For comparison, we extend the implementation of Stereo-Selective Whitening (SSW) in FCStereo [27] to the setting of MVS. FCStereo is a pioneering work in domain generalized stereo with 2 camera settings, which provides a robust baseline for comparison in the table. IBN [37] and EFDM [58] are state-of-the-art domain generalization modules that can be directly plugged into the backbone network. Since our proposed RobustMVS only insert several instance normalization layers into the backbone network, it can provide a direct and fair comparison between our proposed method and these plug-in domain generalization modules. The same backbone network of CasMVSNet [3] is used. We report the quantitative results of cross-domain generalization MVS on 16 different tracks in the table. The source domain and target domain is respectively selected from: **DT**, **BL**, **GS**, and **PA**. From the direct comparison between FCStereo and our method, our method can significantly improve the reconstruction performance that provides a better multi-view feature-whitening based solution for domain generalization in MVS. Moreover, our method can

also outperform other domain generalized baselines like IBN and EFDM on the metric of Overall in **DT** and F-score in **BL**, **GS**, and **PA**. The qualitative results presents the comparison on some reconstructed samples in Fig. 6. Some examples of **GS** \rightarrow **DT** and **GS** \rightarrow **PA** are shown in the figure. From the figure, it can be found that our method can reconstruct better 3D point cloud compared with other method, and suffer less from the distribution gap when generalizing from synthetic domain **GS** to realistic domains.

G. Generalization on Tanks&Temples

The generalization results on **TT** evaluation set are provided in Table III. F-score is used to measure the performance of reconstruction results. The intermediate and advanced sets of **TT** are both utilized for evaluation following previous works [10], [60]. The compared methods include: COLMAP [63], MVSNet [1], R-MVSNet [6], CIDER [64], PatchMatchNet [59], PatchMatchRL [65], VisMVSNet [53], IterMVS [60], CasMVSNet [3], and TransMVSNet [10]. The open-sourced pretrained model of the compared methods are utilized for evaluation. RobustMVS-Cas and RobustMVS-Trans respectively adopts CasMVSNet and TransMVSNet as the backbone network in our RobustMVS framework. The criteria for

TABLE II

QUANTITATIVE COMPARISON WITH DOMAIN GENERALIZATION METHODS UTILIZING **DT**/**BL**/**GS**/**TT** AS SOURCE DOMAIN. BEST RESULTS ARE IN BOLD.

| Methods | DT → DT | | | DT → BL | | | DT → GS | | | DT → PA | | |
|----------------------|----------------|---------------|---------------|----------------|--------------|--------------|----------------|--------------|--------------|----------------|---------------|--------------|
| | Acc.↓ | Comp.↓ | Overall↓ | Prec.↑ | Reca.↑ | F-score↑ | Prec.↑ | Reca.↑ | F-score↑ | Prec.↑ | Reca.↑ | F-score↑ |
| Baseline [3] | 0.325 | 0.385 | 0.355 | 48.21 | 39.91 | 39.06 | 42.99 | 36.93 | 38.74 | 42.61 | 41.76 | 40.78 |
| FCStereo [27] | 0.3332 | 0.3673 | 0.3503 | 49.80 | 42.35 | 40.76 | 43.09 | 38.99 | 40.42 | 52.88 | 46.73 | 48.44 |
| IBN [37] | 0.3284 | 0.3823 | 0.3554 | 46.22 | 42.35 | 39.52 | 46.20 | 41.34 | 42.73 | 55.32 | 49.26 | 50.80 |
| EFDM [62] | 0.3218 | 0.3746 | 0.3482 | 45.78 | 41.67 | 39.35 | 46.02 | 40.44 | 42.19 | 56.16 | 47.98 | 50.71 |
| RobustMVS-Cas | 0.3209 | 0.3634 | 0.3421 | 52.07 | 42.91 | 42.72 | 45.45 | 44.08 | 43.85 | 56.74 | 49.99 | 52.03 |
| Methods | BL → DT | | | BL → BL | | | BL → GS | | | BL → PA | | |
| | Acc.↓ | Comp.↓ | Overall↓ | Prec.↑ | Reca.↑ | F-score↑ | Prec.↑ | Reca.↑ | F-score↑ | Prec.↑ | Reca.↑ | F-score↑ |
| Baseline [3] | 0.4343 | 0.6874 | 0.5608 | 44.91 | 37.60 | 36.44 | 52.67 | 55.69 | 53.42 | 35.44 | 30.22 | 31.06 |
| FCStereo [27] | 0.3534 | 0.3833 | 0.3684 | 44.03 | 43.87 | 38.65 | 53.44 | 55.32 | 53.69 | 37.29 | 31.86 | 32.51 |
| IBN [37] | 0.3490 | 0.3880 | 0.3685 | 44.66 | 46.73 | 40.54 | 53.67 | 54.95 | 53.66 | 33.80 | 26.36 | 28.03 |
| EFDM [62] | 0.3603 | 0.3844 | 0.3723 | 44.40 | 46.09 | 39.89 | 55.38 | 56.42 | 55.19 | 34.56 | 30.28 | 30.68 |
| RobustMVS-Cas | 0.3484 | 0.3820 | 0.3652 | 47.06 | 46.41 | 41.82 | 56.14 | 56.33 | 55.50 | 40.03 | 36.101 | 36.09 |
| Methods | GS → DT | | | GS → BL | | | GS → GS | | | GS → PA | | |
| | Acc.↓ | Comp.↓ | Overall↓ | Prec.↑ | Reca.↑ | F-score↑ | Prec.↑ | Reca.↑ | F-score↑ | Prec.↑ | Reca.↑ | F-score↑ |
| Baseline [3] | 0.5083 | 0.9305 | 0.7194 | 43.20 | 33.51 | 33.15 | 52.59 | 55.27 | 53.23 | 38.63 | 25.48 | 28.81 |
| FCStereo [27] | 0.4411 | 0.7490 | 0.5951 | 41.19 | 36.62 | 34.03 | 52.44 | 56.17 | 53.64 | 37.90 | 28.75 | 30.90 |
| IBN [37] | 0.4531 | 0.7195 | 0.5863 | 44.87 | 37.42 | 36.49 | 50.92 | 56.72 | 52.85 | 45.83 | 32.82 | 36.37 |
| EFDM [62] | 0.4084 | 0.5728 | 0.4906 | 44.12 | 38.33 | 36.80 | 51.00 | 56.14 | 52.76 | 34.66 | 27.01 | 28.47 |
| RobustMVS-Cas | 0.3767 | 0.5390 | 0.4579 | 47.78 | 43.46 | 41.53 | 56.38 | 58.72 | 56.92 | 48.00 | 39.59 | 41.27 |
| Methods | TT → DT | | | TT → BL | | | TT → GS | | | TT → PA | | |
| | Acc.↓ | Comp.↓ | Overall↓ | Prec.↑ | Reca.↑ | F-score↑ | Prec.↑ | Reca.↑ | F-score↑ | Prec.↑ | Reca.↑ | F-score↑ |
| Baseline [3] | 0.4573 | 0.6505 | 0.5539 | 42.80 | 29.70 | 30.83 | 43.74 | 45.41 | 43.67 | 36.59 | 15.62 | 20.67 |
| FCStereo [27] | 0.3721 | 0.5678 | 0.4700 | 44.52 | 30.02 | 31.17 | 43.53 | 45.80 | 43.83 | 38.27 | 17.64 | 22.79 |
| IBN [37] | 0.4598 | 0.5917 | 0.5257 | 43.91 | 31.91 | 32.99 | 43.92 | 46.01 | 44.23 | 35.57 | 21.51 | 25.46 |
| EFDM [62] | 0.3934 | 0.5635 | 0.4784 | 40.63 | 30.27 | 30.79 | 40.37 | 44.64 | 41.54 | 32.71 | 14.76 | 19.32 |
| RobustMVS-Cas | 0.3687 | 0.5320 | 0.4504 | 47.01 | 32.45 | 34.33 | 46.42 | 46.95 | 47.13 | 43.12 | 25.20 | 30.21 |

TABLE III

GENERALIZATION RESULTS TO **TT** EVALUATION BENCHMARK.

| Methods | DT → TT | | BL → TT | |
|------------------------|----------------|--------------|----------------|--------------|
| | Intermediate↑ | Advanced↑ | Intermediate↑ | Advanced↑ |
| COLMAP [63] | 42.14 | 27.24 | 42.14 | 27.24 |
| MVSNet [11] | 43.38 | - | - | - |
| R-MVSNet [6] | 48.4 | 24.91 | - | - |
| CIDER [64] | 46.76 | 23.12 | - | - |
| PatchMatchNet [59] | 53.15 | 32.31 | - | - |
| PatchMatchRL [65] | - | - | 51.81 | 31.78 |
| VisMVSNet [53] | - | - | 60.03 | 33.78 |
| IterMVS [60] | 56.22 | 33.24 | 56.94 | 34.17 |
| CasMVSNet [3] | 56.84 | 31.12 | 57.22 | 32.63 |
| TransMVSNet [10] | 55.0 | 30.2 | 60.3 | 35.3 |
| RobustMVS-Cas | 57.53 | 32.68 | 58.49 | 33.61 |
| RobustMVS-Trans | 57.43 | 31.17 | 60.80 | 36.66 |

TABLE IV

IMPROVEMENT OF GENERALIZATION RESULTS TO **TT** EVALUATION BENCHMARK WITH THE SAME BACKBONE, CASMVSNET [3].

| Methods | DT → TT | | BL → TT | |
|-------------------------------------|----------------|-----------|----------------|-----------|
| | Intermediate↑ | Advanced↑ | Intermediate↑ | Advanced↑ |
| Baseline [3] | 56.84 | 31.12 | 57.22 | 32.63 |
| RobustMVS-Cas (Δ^\uparrow) | +0.69 | +1.56 | +1.27 | +0.98 |
| Methods | GS → TT | | TT → TT | |
| | Intermediate↑ | Advanced↑ | Intermediate↑ | Advanced↑ |
| Baseline [3] | 44.65 | 22.61 | 47.07 | 26.55 |
| RobustMVS-Cas (Δ^\uparrow) | +8.91 | +7.1 | +2.85 | +0.95 |

choosing these networks as baselines is to compare the single domain generalization performance in a comparative setting. Since TransMVSNet adopts multiple datasets (**DT** + **BL**) for training, we use their official implementation to retrain the network on single domain respectively to ensure a fair comparison in the single domain generalization benchmark. In the table, the performance of **DT** → **TT** and **BL** → **TT** are reported for comparison. As the results show, our RobustMVS-Trans

outperforms the baseline TransMVSNet on the intermediate and advanced set in both 2 settings. Superior results can also be witnessed in the comparison between RobustMVS-Cas and the baseline CasMVSNet. When compared with other methods, our RobustMVS can still have competitive performance and even better results.

In Table IV, we further provide the improvement of generalization results towards **TT** dataset in evaluation. The same backbone of CasMVSNet is adopted here. The evaluation includes 4 different tracks: **DT** → **TT**, **BL** → **TT**, **GS** → **TT**, and **TT** → **TT**. It can be explored that the RobustMVS can improve the performance on all these benchmarks in both the intermediate and advanced set. Furthermore, when the synthetic dataset **GS** is used as source domain, significant improvement can be witnessed on intermediate set (+8.91) and advanced set (+7.1).

H. Ablation Study

1) **Ablation Analysis of Different Components:** To evaluate the effectiveness of each component in the proposed RobustMVS framework, we conduct ablation experiments on them and provide the quantitative results in Table V. In the table we present the results on 3 different tracks: **DT** → **BL**, **DT** → **GS**, and **DT** → **PA**. The backbone network is CasMVSNet in default. The "baseline" represents that the original CasMVSNet network. "DCW" means the proposed DCW-loss is appended in the training phase. "IN" and "DA" respectively represents the instance normalization module in the network and data augmentation strategy during training. As the table shows, when DCW-loss is appended to the MVS network training, the F-score is improved on all 3 benchmarks.

TABLE V
ABLATION RESULTS OF DIFFERENT COMPONENTS IN ROBUSTMVS.

| Components | | | | DT → BL | | | DT → GS | | | DT → PA | | |
|------------|-----|----|----|--------------|--------------|--------------|--------------|--------------|--------------|--------------|--------------|--------------|
| Baseline | DCW | IN | DA | Prec.↑ | Reca.↑ | F-score↑ | Prec.↑ | Reca.↑ | F-score↑ | Prec.↑ | Reca.↑ | F-score↑ |
| ✓ | | | | 48.21 | 39.91 | 39.06 | 42.99 | 36.93 | 38.74 | 42.61 | 41.76 | 40.78 |
| ✓ | ✓ | | | 48.20 | 41.44 | 39.70 | 44.33 | 39.28 | 40.65 | 51.31 | 46.49 | 47.51 |
| ✓ | ✓ | ✓ | | 51.80 | 42.07 | 41.94 | 47.10 | 37.69 | 41.03 | 47.04 | 57.95 | 51.55 |
| ✓ | ✓ | ✓ | ✓ | 52.07 | 42.91 | 42.72 | 45.45 | 44.08 | 43.85 | 56.74 | 49.99 | 52.03 |

TABLE VI
ABLATION EXPERIMENTS OF THE NUMBER OF DEPTH CLUSTERS K . GS (SYNTHETIC DATA) IS USED AS SOURCE DOMAIN.

| Depth clusters | GS → DT | | | GS → BL | | | GS → GS | | | GS → PA | | |
|----------------|---------------|---------------|---------------|--------------|--------------|--------------|--------------|--------------|--------------|--------------|--------------|--------------|
| | Acc.↓ | Comp.↓ | Overall↓ | Prec.↑ | Reca.↑ | F-score↑ | Prec.↑ | Reca.↑ | F-score↑ | Prec.↑ | Reca.↑ | F-score↑ |
| K=0 | 0.4411 | 0.7490 | 0.5951 | 41.19 | 36.62 | 34.03 | 52.44 | 56.17 | 53.64 | 37.90 | 28.75 | 30.90 |
| K=4 | 0.4148 | 0.4148 | 0.5122 | 44.92 | 40.00 | 38.53 | 54.02 | 57.91 | 55.27 | 39.72 | 33.59 | 34.63 |
| K=6 | 0.3886 | 0.6315 | 0.5101 | 46.51 | 42.28 | 40.40 | 55.51 | 58.53 | 56.41 | 42.27 | 36.11 | 37.44 |
| K=8 | 0.3767 | 0.5390 | 0.4579 | 47.78 | 43.46 | 41.53 | 56.38 | 58.72 | 56.92 | 48.00 | 39.59 | 41.27 |
| K=10 | 0.4087 | 0.5993 | 0.5040 | 43.51 | 38.24 | 36.19 | 52.64 | 56.07 | 53.67 | 42.11 | 33.25 | 35.34 |
| K=12 | 0.4141 | 0.6085 | 0.5113 | 41.00 | 38.24 | 35.62 | 52.45 | 57.08 | 54.03 | 33.45 | 30.64 | 30.88 |
| K=14 | 0.4372 | 0.5953 | 0.5162 | 40.93 | 36.64 | 34.35 | 50.78 | 56.34 | 52.71 | 33.84 | 26.88 | 27.89 |

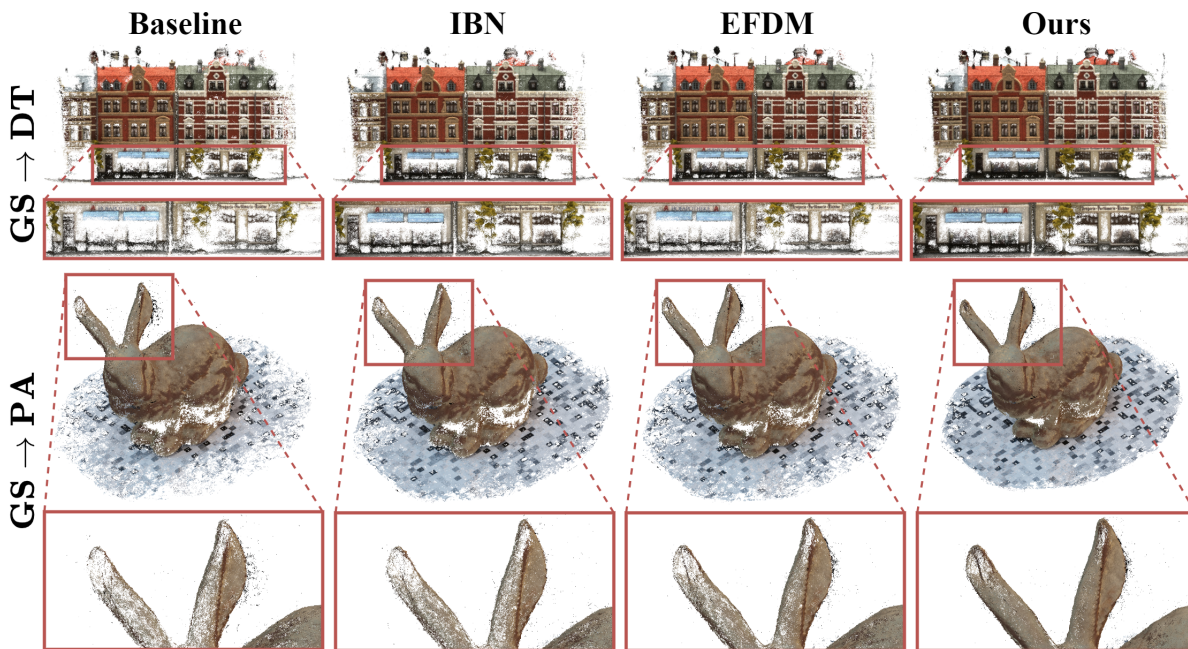


Fig. 6. Qualitative comparison with domain generalization methods utilizing GS as source domain.

Since the Instance Normalization is usually paired with the whitening loss, better performance can be achieved when IN is also used. The involvement of data-augmentation strategy enables the feature whitening loss to reduce the domain bias under more various scenarios compared with the naive setting. As the table shows, each component is effective in improving the generalization performance.

2) Ablation Analysis of Different Clusters: To explore the effectiveness of the depth clusters K in DCW loss, we also conduct ablation experiments for different settings: $K_{clu} = 0/4/6/8/10/12/14$ on the benchmark of **GS → DT**, **GS → BL**, **GS → GS**, and **GS → PA**. When $K_{clu} = 0$, it represents the basic feature whitening loss used in FC Stereo [27]. When K_{clu} is larger than 0, it represents the depth cluster used

in our DCW-loss. As shown in Table VI, the performance improves when K_{clu} is smaller than 8 but degrades when K_{clu} becomes larger than 8. The reason is that K_{clu} is small, increasing the number of clusters can regularize the cross-view correspondence in a more detailed local region. However, when K_{clu} becomes too large, the pixels located in the local corresponding regions contains less variance of style information, which tends to have smaller difference among each other. Thus the regularization on these small regions can not effectively excavate the style information when calculating feature whitening loss, and degrade the reconstruction performance.

There are a few suggestions if you want to adjust the depth cluster number (K_{clu}) when the image resolution (H ,

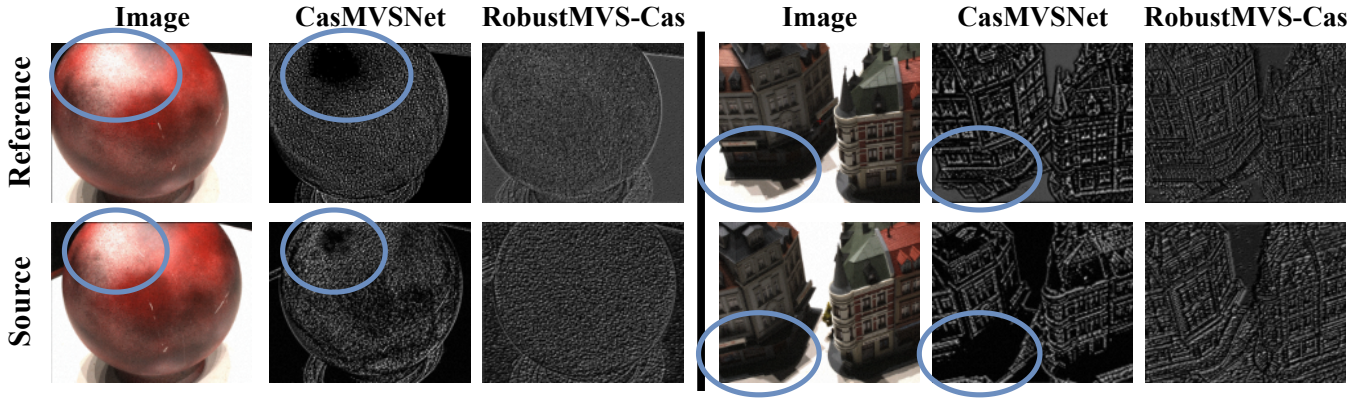


Fig. 7. Grad-cam [16] visualization example of RobustMVS under domain generalization setting of **GS** \rightarrow **DT**.

W) changes: a) If the image resolution is similar in scale to the default setting in our synthetic domain (640×480 in **GS**), you can use the default setting of (K_{clu}), i.e. **DT** (640×512). b) If the difference between the image resolutions of the target dataset and the default synthetic dataset **GS** is too large, we suggest downsampling the image resolution to a comparative scale of the default one. For example, the image resolution of **TT** can be resized to 640×480 from its original one for training. c) The depth cluster number choice may also be affected by the variety of depth values in a scene (synthetic or real). This is because the balanced distance-based metric in K-Means may be affected by the sparsity of point clouds. For example, for some sharp shapes vertical to the image plane, the sampled points from depth might be pretty sparse. In point clouds, K-Means clustering might ignore these sparse points and focus on the dense points with flat shapes horizontal to the image plane. This problem might occur when the image resolution is relatively small. We can mitigate it by not shrinking the image resolution. d) We suggest not setting K_{clu} to be larger than 8 as training might become unstable and return NaN values caused by the strong whitening constraints. Finally, due to the implementation issue in parallelism, we utilize an even number of depth clusters for parallelizing the computation.

3) Grad-cam visualization of MVS: To explain the effectiveness of the proposed RobustMVS framework, we provide the Grad-cam [16] visualization results in Fig. 7. We compare the baseline model of CasMVSNet and RobustMVS-Cas for visualization. In default the source domain is synthetic dataset **GS** and the target domain is **DT**. The error between the estimated depth map of the MVS network and the ground truth depth is back-propagated to the convolutional layers, we utilize Grad-cam [16] to visualize the gradient on feature maps. In the first column, the original images of the reference view and source view are shown. The second and third column respectively show the activation map of baseline model and our proposed method. The blue circle in the figure points out the ignored activation areas in the baseline model. For example, in the left example, the light exposure results in textureless regions on the red ball, which has never been seen before in the synthetic dataset **GS**. Consequently, the baseline model

TABLE VII
COMPARISON OF COMPUTATION EFFICIENCY. THE INFERENCE TIME IS EVALUATED ON A SINGLE A100 GPU.

| Methods | Params | GFLOPS | Inference Time (s) |
|---------------|----------|----------|--------------------|
| CasMVSNet | 934.304K | 268.540G | 0.1904 |
| RobustMVS-Cas | 934.192K | 268.401G | 0.1977 |

can not handle this case and these areas are not activated in blue circles. However, our RobustMVS can provide more complete activation map compared with baseline model on the whole activation map. From these examples, we can find that our RobustMVS provide a robust regularization to reduce the domain bias and maintain a well-distributed feature activation map across domains.

4) Computation efficiency: We have compared the baseline of CasMVSNet with our RobustMVS-Cas, and the results are presented in Table VII. Both networks use the same backbone, but our RobustMVS-Cas replaces some BN layers with IN layers. Our RobustMVS-Cas has slightly fewer parameters and lower GFLOPS than the baseline backbone. However, the inference time of RobustMVS-Cas might be slightly slower than the baseline backbone network. This is because the original backbone uses batch normalization layers that can store the running mean and variance values, reducing computation during inference. In contrast, our RobustMVS-Cas requires extra online computation during inference due to the replacement of some batch normalization layers with instance normalization layers. Despite the slightly slower inference time than the baseline, our RobustMVS-Cas can significantly improve the generalization performance.

VI. CONCLUSION

This paper first introduces the domain generalization problem in the field of MVS. As the visualization of the activation map on MVS networks across different domains shows, the bottleneck lies in the robustness towards cross-view matching features across domain-specific conditions. Consequently, we propose a novel domain generalized MVS framework, RobustMVS. It requires little modifications to the backbone MVS network and applies a Depth-Clustering-guided Whitening (DCW) loss to diminish the domain-specific styles on spatially

neighboring regions. We extend the MVS evaluation benchmarks to 5 datasets for domain generalization and compare the proposed method with existing MVS methods and domain generalization methods. The experimental results reveal the robust performance of the proposed method in the domain generalization benchmark of MVS. The final visualization of activation maps in our proposed method gives clues to indicate whether it can reduce the influence of domain bias. For future work, we will explore the further extension of Transformer-based MVS networks in the domain generalized MVS tasks and try to conduct domain generalization from large-scale synthetic MVS datasets towards realistic MVS datasets.

REFERENCES

- [1] Y. Yao, Z. Luo, S. Li, T. Fang, and L. Quan, "Mvsnet: Depth inference for unstructured multi-view stereo," in *Proceedings of the European conference on computer vision (ECCV)*, 2018, pp. 767–783.
- [2] R. T. Collins, "A space-sweep approach to true multi-image matching," in *Proceedings CVPR IEEE Computer Society Conference on Computer Vision and Pattern Recognition*. Ieee, 1996, pp. 358–363.
- [3] X. Gu, Z. Fan, S. Zhu, Z. Dai, F. Tan, and P. Tan, "Cascade cost volume for high-resolution multi-view stereo and stereo matching," in *Proceedings of the IEEE/CVF Conference on Computer Vision and Pattern Recognition*, 2020, pp. 2495–2504.
- [4] S. Cheng, Z. Xu, S. Zhu, Z. Li, L. E. Li, R. Ramamoorthi, and H. Su, "Deep stereo using adaptive thin volume representation with uncertainty awareness," in *Proceedings of the IEEE/CVF Conference on Computer Vision and Pattern Recognition*, 2020, pp. 2524–2534.
- [5] R. Peng, R. Wang, Z. Wang, Y. Lai, and R. Wang, "Rethinking depth estimation for multi-view stereo: A unified representation," in *Proceedings of the IEEE/CVF Conference on Computer Vision and Pattern Recognition*, 2022, pp. 8645–8654.
- [6] Y. Yao, Z. Luo, S. Li, T. Shen, T. Fang, and L. Quan, "Recurrent mvsnet for high-resolution multi-view stereo depth inference," in *Proceedings of the IEEE/CVF conference on computer vision and pattern recognition*, 2019, pp. 5525–5534.
- [7] T. Khot, S. Agrawal, S. Tulsiani, C. Mertz, S. Lucey, and M. Hebert, "Learning unsupervised multi-view stereopsis via robust photometric consistency," *arXiv preprint arXiv:1905.02706*, 2019.
- [8] B. Huang, H. Yi, C. Huang, Y. He, J. Liu, and X. Liu, "M3vsnet: Unsupervised multi-metric multi-view stereo network," in *2021 IEEE International Conference on Image Processing (ICIP)*. IEEE, 2021, pp. 3163–3167.
- [9] H. Xu, Z. Zhou, Y. Qiao, W. Kang, and Q. Wu, "Self-supervised multi-view stereo via effective co-segmentation and data-augmentation," in *Proceedings of the AAAI Conference on Artificial Intelligence*, vol. 35, no. 4, 2021, pp. 3030–3038.
- [10] Y. Ding, W. Yuan, Q. Zhu, H. Zhang, X. Liu, Y. Wang, and X. Liu, "Transmvsnet: Global context-aware multi-view stereo network with transformers," in *Proceedings of the IEEE/CVF Conference on Computer Vision and Pattern Recognition*, 2022, pp. 8585–8594.
- [11] R. Jensen, A. Dahl, G. Vogiatzis, E. Tola, and H. Aanæs, "Large scale multi-view stereopsis evaluation," in *Proceedings of the IEEE conference on computer vision and pattern recognition*, 2014, pp. 406–413.
- [12] Y. Yao, Z. Luo, S. Li, J. Zhang, Y. Ren, L. Zhou, T. Fang, and L. Quan, "Blendedmvs: A large-scale dataset for generalized multi-view stereo networks," in *Proceedings of the IEEE/CVF Conference on Computer Vision and Pattern Recognition*, 2020, pp. 1790–1799.
- [13] K. Wang and S. Shen, "Flow-motion and depth network for monocular stereo and beyond," *IEEE Robotics and Automation Letters*, vol. 5, no. 2, pp. 3307–3314, 2020.
- [14] A. Broekman and P. J. Gräbe, "Pasmvs: a perfectly accurate, synthetic, path-traced dataset featuring specular material properties for multi-view stereopsis training and reconstruction applications," *Data in brief*, vol. 32, p. 106219, 2020.
- [15] A. Knapitsch, J. Park, Q.-Y. Zhou, and V. Koltun, "Tanks and temples: Benchmarking large-scale scene reconstruction," *ACM Transactions on Graphics (ToG)*, vol. 36, no. 4, pp. 1–13, 2017.
- [16] R. R. Selvaraju, M. Cogswell, A. Das, R. Vedantam, D. Parikh, and D. Batra, "Grad-cam: Visual explanations from deep networks via gradient-based localization," in *Proceedings of the IEEE international conference on computer vision*, 2017, pp. 618–626.
- [17] S. Ben-David, J. Blitzer, K. Crammer, and F. Pereira, "Analysis of representations for domain adaptation," *Advances in neural information processing systems*, vol. 19, 2006.
- [18] Y. Ganin and V. Lempitsky, "Unsupervised domain adaptation by back-propagation," in *International conference on machine learning*. PMLR, 2015, pp. 1180–1189.
- [19] J. Hoffman, E. Tzeng, T. Park, J.-Y. Zhu, P. Isola, K. Saenko, A. Efros, and T. Darrell, "Cycada: Cycle-consistent adversarial domain adaptation," in *International conference on machine learning*. Pmlr, 2018, pp. 1989–1998.
- [20] X. Ye, J. Zhang, Y. Yuan, R. Xu, Z. Wang, and H. Li, "Underwater depth estimation via stereo adaptation networks," *IEEE Transactions on Circuits and Systems for Video Technology*, 2023.
- [21] K. Muandet, D. Balduzzi, and B. Schölkopf, "Domain generalization via invariant feature representation," in *International Conference on Machine Learning*. PMLR, 2013, pp. 10–18.
- [22] H. Li, S. J. Pan, S. Wang, and A. C. Kot, "Domain generalization with adversarial feature learning," in *Proceedings of the IEEE conference on computer vision and pattern recognition*, 2018, pp. 5400–5409.
- [23] Y. Li, X. Tian, M. Gong, Y. Liu, T. Liu, K. Zhang, and D. Tao, "Deep domain generalization via conditional invariant adversarial networks," in *Proceedings of the European Conference on Computer Vision (ECCV)*, 2018, pp. 624–639.
- [24] C. Cai, M. Poggi, S. Mattoccia, and P. Mordohai, "Matching-space stereo networks for cross-domain generalization," in *2020 International Conference on 3D Vision (3DV)*. IEEE, 2020, pp. 364–373.
- [25] F. Zhang, X. Qi, R. Yang, V. Prisacariu, B. Wah, and P. Torr, "Domain-invariant stereo matching networks," in *European Conference on Computer Vision*. Springer, 2020, pp. 420–439.
- [26] Z. Shen, Y. Dai, and Z. Rao, "Cfnet: Cascade and fused cost volume for robust stereo matching," in *Proceedings of the IEEE/CVF Conference on Computer Vision and Pattern Recognition*, 2021, pp. 13 906–13 915.
- [27] J. Zhang, X. Wang, X. Bai, C. Wang, L. Huang, Y. Chen, L. Gu, J. Zhou, T. Harada, and E. R. Hancock, "Revisiting domain generalized stereo matching networks from a feature consistency perspective," in *Proceedings of the IEEE/CVF Conference on Computer Vision and Pattern Recognition*, 2022, pp. 13 001–13 011.
- [28] H. Dai, X. Zhang, Y. Zhao, H. Sun, and N. Zheng, "Adaptive disparity candidates prediction network for efficient real-time stereo matching," *IEEE Transactions on Circuits and Systems for Video Technology*, vol. 32, no. 5, pp. 3099–3110, 2022.
- [29] Z. Lu, J. Wang, Z. Li, S. Chen, and F. Wu, "A resource-efficient pipelined architecture for real-time semi-global stereo matching," *IEEE Transactions on Circuits and Systems for Video Technology*, vol. 32, no. 2, pp. 660–673, 2022.
- [30] B. Pan, L. Zhang, and H. Wang, "Multi-stage feature pyramid stereo network-based disparity estimation approach for two to three-dimensional video conversion," *IEEE Transactions on Circuits and Systems for Video Technology*, vol. 31, no. 5, pp. 1862–1875, 2021.
- [31] L. Gatys, A. S. Ecker, and M. Bethge, "Texture synthesis using convolutional neural networks," *Advances in neural information processing systems*, vol. 28, 2015.
- [32] L. A. Gatys, A. S. Ecker, and M. Bethge, "Image style transfer using convolutional neural networks," in *Proceedings of the IEEE conference on computer vision and pattern recognition*, 2016, pp. 2414–2423.
- [33] X. Pan, X. Zhan, J. Shi, X. Tang, and P. Luo, "Switchable whitening for deep representation learning," in *Proceedings of the IEEE/CVF International Conference on Computer Vision*, 2019, pp. 1863–1871.
- [34] P. Luo, "Learning deep architectures via generalized whitened neural networks," in *International Conference on Machine Learning*. PMLR, 2017, pp. 2238–2246.
- [35] B. Sun and K. Saenko, "Deep coral: Correlation alignment for deep domain adaptation," in *European conference on computer vision*. Springer, 2016, pp. 443–450.
- [36] S. Choi, S. Jung, H. Yun, J. T. Kim, S. Kim, and J. Choo, "Robustnet: Improving domain generalization in urban-scene segmentation via instance selective whitening," in *Proceedings of the IEEE/CVF Conference on Computer Vision and Pattern Recognition*, 2021, pp. 11 580–11 590.
- [37] X. Pan, P. Luo, J. Shi, and X. Tang, "Two at once: Enhancing learning and generalization capacities via ibn-net," in *Proceedings of the European Conference on Computer Vision (ECCV)*, 2018, pp. 464–479.
- [38] S. Galliani, K. Lasinger, and K. Schindler, "Massively parallel multiview stereopsis by surface normal diffusion," in *Proceedings of the IEEE International Conference on Computer Vision*, 2015, pp. 873–881.
- [39] N. D. Campbell, G. Vogiatzis, C. Hernández, and R. Cipolla, "Using multiple hypotheses to improve depth-maps for multi-view stereo," in *Computer Vision—ECCV 2008: 10th European Conference on Computer*

- Vision, Marseille, France, October 12-18, 2008, Proceedings, Part I 10. Springer, 2008, pp. 766–779.
- [40] Y. Furukawa and J. Ponce, “Accurate, dense, and robust multiview stereopsis,” *IEEE Transactions on Pattern Analysis and Machine Intelligence*, vol. 32, no. 8, pp. 1362–1376, 2010.
- [41] J. Yan, Z. Wei, H. Yi, M. Ding, R. Zhang, Y. Chen, G. Wang, and Y.-W. Tai, “Dense hybrid recurrent multi-view stereo net with dynamic consistency checking,” in *European conference on computer vision*, Springer, 2020, pp. 674–689.
- [42] Z. Wei, Q. Zhu, C. Min, Y. Chen, and G. Wang, “Aa-rmvsnet: Adaptive aggregation recurrent multi-view stereo network,” in *Proceedings of the IEEE/CVF International Conference on Computer Vision*, 2021, pp. 6187–6196.
- [43] J. Yang, W. Mao, J. M. Alvarez, and M. Liu, “Cost volume pyramid based depth inference for multi-view stereo,” in *Proceedings of the IEEE/CVF Conference on Computer Vision and Pattern Recognition*, 2020, pp. 4877–4886.
- [44] W. Su, Q. Xu, and W. Tao, “Uncertainty guided multi-view stereo network for depth estimation,” *IEEE Transactions on Circuits and Systems for Video Technology*, vol. 32, no. 11, pp. 7796–7808, 2022.
- [45] R. Zhao, X. Han, X. Guo, L. Kuang, X. Yang, and F. Sun, “Exploring the point feature relation on point cloud for multi-view stereo,” *IEEE Transactions on Circuits and Systems for Video Technology*, vol. 33, no. 11, pp. 6747–6763, 2023.
- [46] H. Zhang, X. Ye, S. Chen, Z. Wang, H. Li, and W. Ouyang, “The farther the better: Balanced stereo matching via depth-based sampling and adaptive feature refinement,” *IEEE Transactions on Circuits and Systems for Video Technology*, vol. 32, no. 7, pp. 4613–4625, 2021.
- [47] X. Wang, Z. Zhu, G. Huang, F. Qin, Y. Ye, Y. He, X. Chi, and X. Wang, “Mvster: Epipolar transformer for efficient multi-view stereo,” in *European Conference on Computer Vision*. Springer, 2022, pp. 573–591.
- [48] A. Vaswani, N. Shazeer, N. Parmar, J. Uszkoreit, L. Jones, A. N. Gomez, L. Kaiser, and I. Polosukhin, “Attention is all you need,” *Advances in neural information processing systems*, vol. 30, 2017.
- [49] H. Xu, Z. Zhou, Y. Wang, W. Kang, B. Sun, H. Li, and Y. Qiao, “Digging into uncertainty in self-supervised multi-view stereo,” in *Proceedings of the IEEE/CVF International Conference on Computer Vision*, 2021, pp. 6078–6087.
- [50] A. Mallick, J. Stückler, and H. P. Lensch, “Learning to adapt multi-view stereo by self-supervision,” in *BMVC*, vol. 1, 2020, p. 2.
- [51] S. Chen, Z. Pu, X. Fan, and B. Zou, “Fixing defect of photometric loss for self-supervised monocular depth estimation,” *IEEE Transactions on Circuits and Systems for Video Technology*, vol. 32, no. 3, pp. 1328–1338, 2021.
- [52] Y. Wei, H. Guo, J. Lu, and J. Zhou, “Iterative feature matching for self-supervised indoor depth estimation,” *IEEE Transactions on Circuits and Systems for Video Technology*, vol. 32, no. 6, pp. 3839–3852, 2021.
- [53] J. Zhang, Y. Yao, S. Li, Z. Luo, and T. Fang, “Visibility-aware multi-view stereo network,” *arXiv preprint arXiv:2008.07928*, 2020.
- [54] W. Cho, S. Choi, D. K. Park, I. Shin, and J. Choo, “Image-to-image translation via group-wise deep whitening-and-coloring transformation,” in *Proceedings of the IEEE/CVF Conference on Computer Vision and Pattern Recognition*, 2019, pp. 10 639–10 647.
- [55] Y. Li, C. Fang, J. Yang, Z. Wang, X. Lu, and M.-H. Yang, “Universal style transfer via feature transforms,” *Advances in neural information processing systems*, vol. 30, 2017.
- [56] D. Ulyanov, A. Vedaldi, and V. Lempitsky, “Instance normalization: The missing ingredient for fast stylization,” *arXiv preprint arXiv:1607.08022*, 2016.
- [57] J. A. Hartigan and M. A. Wong, “Algorithm as 136: A k-means clustering algorithm,” *Journal of the royal statistical society. series c (applied statistics)*, vol. 28, no. 1, pp. 100–108, 1979.
- [58] H. Xu, Z. Zhou, W. Cheng, B. Sun, H. Li, and W. Kang, “Semi-supervised deep multi-view stereo,” *arXiv preprint arXiv:2207.11699*, 2022.
- [59] F. Wang, S. Galliani, C. Vogel, P. Speciale, and M. Pollefeys, “Patchmatchnet: Learned multi-view patchmatch stereo,” in *Proceedings of the IEEE/CVF Conference on Computer Vision and Pattern Recognition*, 2021, pp. 14 194–14 203.
- [60] F. Wang, S. Galliani, C. Vogel, and M. Pollefeys, “Itermvs: Iterative probability estimation for efficient multi-view stereo,” in *Proceedings of the IEEE/CVF Conference on Computer Vision and Pattern Recognition*, 2022, pp. 8606–8615.
- [61] K. T. Giang, S. Song, and S. Jo, “Curvature-guided dynamic scale networks for multi-view stereo,” *arXiv preprint arXiv:2112.05999*, 2021.

- [62] Y. Zhang, M. Li, R. Li, K. Jia, and L. Zhang, “Exact feature distribution matching for arbitrary style transfer and domain generalization,” in *Proceedings of the IEEE/CVF Conference on Computer Vision and Pattern Recognition*, 2022, pp. 8035–8045.
- [63] J. L. Schonberger and J.-M. Frahm, “Structure-from-motion revisited,” in *Proceedings of the IEEE conference on computer vision and pattern recognition*, 2016, pp. 4104–4113.
- [64] Q. Xu and W. Tao, “Learning inverse depth regression for multi-view stereo with correlation cost volume,” in *Proceedings of the AAAI Conference on Artificial Intelligence*, vol. 34, no. 07, 2020, pp. 12 508–12 515.
- [65] J. Y. Lee, J. DeGol, C. Zou, and D. Hoiem, “Patchmatch-rl: Deep mvs with pixelwise depth, normal, and visibility,” in *Proceedings of the IEEE/CVF International Conference on Computer Vision*, 2021, pp. 6158–6167.



Hongbin Xu received B.E. degree from Nanchang University in 2018 and M.S. degree from South China University of Technology in 2021. He is currently pursuing the Ph.D. degree with the School of Automation Science and Engineering, South China University of Technology, Guangzhou, China. His research interests include 3D vision, 3D reconstruction, and computer vision.



Weitao Chen Weitao Chen received the M.S. degree from Xiamen University, Xiamen, China, in 2016. He is working as a staff/senior algorithm engineer at Tongyi Laboratory, Alibaba Group. His research interests include 3D vision, AIGC, AI4Science and remote sensing.



Baigui Sun Baigui Sun received the M.Eng. degree from Zhejiang University, Hangzhou, China, in 2014. He joined Alibaba Group, Hangzhou, China, as a computer vision algorithm researcher, in 2014. His research interests include face detection/recognition, deep metric learning, domain adaptation, zero/few-shot learning, semi-supervised learning, MVS and computer vision applications. He has published over 26+ articles in international journals and conferences.



Xuansong Xie Xuansong Xie received the PH.D. degree from Jilin University, Jilin, China. He is a senior algorithm expert at Alibaba, serving as the technical director of the Open Vision Intelligence Department at the Tongyi Laboratory. He is also a core member of the Alibaba Group’s visual technology team and responsible for the Alibaba Cloud Vision Intelligence Open Platform. His research interests include visual generation, editing, perception and understanding.



Wenxiong Kang (Member, IEEE) received the M.S. degree from Northwestern Polytechnical University, Xi’an, China, in 2003, and the Ph.D. degree from the South China University of Technology, Guangzhou, China, in 2009. He is currently a Professor with the School of Automation Science and Engineering, South China University of Technology. His research interests include biometrics identification, image processing, pattern recognition, and computer vision.